Uniaxial compression of a yield stress fluid

Thomasina V. Ball
Mathematics Institute, University of Warwick, Coventry CV4 7AL, United Kingdom

(Received 6 May 2026; accepted 21 September 2026; published 2 November 2026)

We characterize a surface instability that occurs when a yield stress fluid is subject to uniaxial compression. We describe experiments using a prestretched elastic sheet which, upon controlled release, uniaxially compresses a layer of petroleum jelly creating surface undulations perpendicular to the direction of compression. We measure experimentally the amplitude and wavelength of the surface undulations, and their dependence on the thickness of the material and the Bingham number, the nondimensional yield stress. Results show that the amplitude of the undulations depends linearly on the Bingham number, whereas the wavelength scales with the initial thickness of the compressed layer. These experiments enhance our understanding of surface instabilities in related systems, such as recent experiments scraping a thin layer of a viscoplastic fluid. Characterizing these surface undulations is integral for geophysical applications in understanding topographic features in accretionary wedges.

DOI: 10.1103/x9t6-4324

I. INTRODUCTION

Recent experiments scraping a uniform, thin film of a yield stress fluid have demonstrated a striking phenomenon: the formation of a surface instability in the form of undulations perpendicular to the direction of compression [1–3]. Experimental images of this phenomenon from Ribinskas *et al.* are reproduced in Figs. 1(a) and 1(b) [2]. The fluids which have been observed to show this behavior (Carbopol 980; Anagel ultrasound gel; and Enliven Hair Gel Extreme, hold 4) have complex elastoviscoplastic behavior, but can be modeled as viscoplastic fluids with a Herschel-Bulkley constitutive law over the strain-rates explored in the experiments. Similar surface undulations have also been seen in numerical simulations of a viscoplastic column collapse [4]. This instability cannot be described with thin film theory since the characteristic wavelength is on the order of the layer thickness [2,3]. In addition, this instability is not observed when a Newtonian fluid is used, suggesting the likely cause is the yield stress.

These observations of surface undulations have strong connections with the geophysical process of thin-skinned mountain building, specifically with fold-and-thrust belts, and their underwater analogues, accretionary prisms. Continuum models can be used to describe large scale topographic features of accretionary prisms: a type of mountain belt formed from sediments accreted onto the overriding tectonic plate at a convergent plate boundary. By nondimensionalizing using timescales on the order of millions of years, direct comparisons between geophysical data and thin film models have been made, reproducing leading order topographic features of such wedges on the scale of hundreds of kilometres [5]. However, mountain ranges such as the Makran accretionary prism [6],

Published by the American Physical Society under the terms of the Creative Commons Attribution 4.0 International license. Further distribution of this work must maintain attribution to the author(s) and the published article's title, journal citation, and DOI.

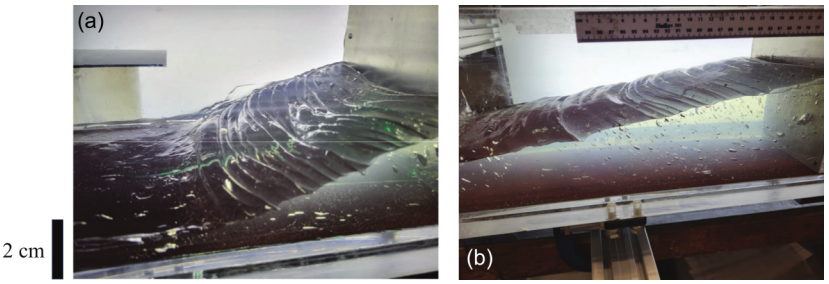


FIG. 1. (a), (b) Images from experiments scraping a uniform layer of viscoplastic fluid (Anagel ultrasound gel), reproduced with permission from Ribinskas *et al.* [2].

and the Indo-Burman Ranges [7], clearly demonstrate short wavelength (tens of kilometres) faults and folds which are not captured by these purely viscous models (e.g., Refs. [8,9]).

The surface instability observed in the analog experiments scraping a viscoplastic fluid bears a stark similarity with these short wavelength features. In terms of modeling mountain building, the introduction of a yield stress to the rheological description allows one to begin to parametrize the ductile and brittle behavior known to occur in the lithosphere (the crust and the upper mantle) [10]. A connection between these geophysical features and the complex rheology of the lithosphere has been made by authors in numerical studies compressing an elastic-perfectly plastic wedge [11,12]. These numerical simulations by Panian and Wiltschko show that the wavelength of the folds observed is strongly dependent on the fluid layer thickness, but the dependence on the rheological model chosen is not explored.

The purpose of this study is to characterize the surface instability observed in experimental studies scraping a yield stress fluid. To do so, it is advantageous to isolate the undulations from the large scale background flow, where there is a balance between advection and gravitational spreading. Hence, we look for inspiration from techniques often used in soft matter physics. To explore surface instabilities in soft materials under compression, a common experiment is to place the sample under consideration on a prestretched elastic sheet. Upon releasing the elastic sheet at a controlled rate, a compressive stress is induced in the sample. The compressive stress is homogeneous over the entire length of the sample, rather than a localized compressive stress that would occur when pushing on one end of the sample. Experiments applying uniaxial compression to viscoelastic fluids have demonstrated a similar surface instability, but on short timescales (e.g., Refs. [13,14]). Mora *et al.* observed that beyond the relaxation time of the material, when the viscoelastic fluid effectively behaves as a viscous fluid, no instability occurred [14]. This type of experiment has also been used to explore creasing in stress-free soft elastomers attached to much thicker and stiffer prestretched substrates (e.g., Refs. [15,16]); and the wrinkling of elastic films on viscous layers compressed by a prestretched elastic substrate (e.g., Refs. [17,18]).

In our experiments presented in this paper we use a different material than in the previous experiments scraping a viscoplastic fluid to attain higher nondimensional yield stresses. In particular we use petroleum jelly, which has been categorized as a viscoplastic fluid beyond a critical stress in the context of cleaning soil layers from surfaces [19,20]. When compressing the petroleum jelly with a prestretched elastic substrate, we control either the compression speed (equivalently the nondimensional yield stress) or the thickness of the fluid layer. In all the experiments we observe that surface undulations form. In our results we characterize this surface instability by measuring how the arc length and wavelength of the undulations evolve in time.

The paper is organized as follows. In Sec. II we outline the experimental procedure and materials used. In Sec. III we present results from experiments varying the speed of compression, and varying the layer thickness. Finally, in Sec. IV we evaluate the results in the context of the previous work, and discuss the limitations of the study, concluding in Sec. V.

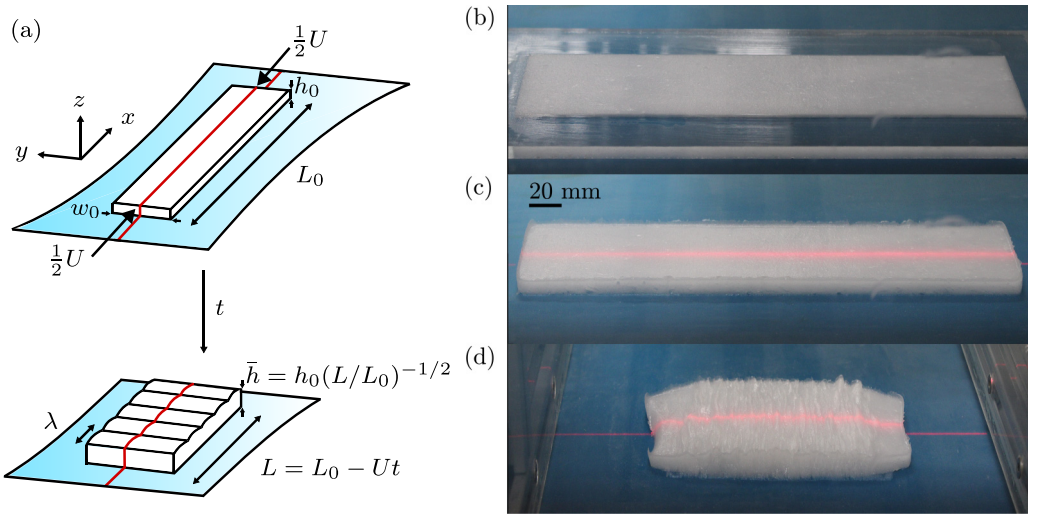


FIG. 2. (a) Schematic of the experimental procedure. The initial sample of volume $h_0 L_0 w_0$ is placed onto an elastic sheet under tension (b), (c). The sample is then compressed with both edges moving at speed $U/2$. The resulting sample (d) with mean height $\bar{h}$ and length L is then detected along the centerline using a laser.

II. EXPERIMENTS

A. Setup

A schematic of the experimental setup is shown in Fig. 2(a). A sample of petroleum jelly was placed onto a rubber sheet under tension. The 30×30 cm sheet is made from rubber latex, with thickness of 0.38 mm (LATXBFQ-620-0.38, PAR Group). This sheet was chosen for its low tensile strength (25 MPa), but large elongation at failure (850%). During the experiments, the maximum elongation was around 100%, and hence we assume the sheet was deforming elastically throughout. The sheet was clamped at the edges between two metal plates; the speed of the edges was controlled with a motor. Assuming a no-slip condition at the base of the sample, we therefore indirectly controlled the motion of the edges of the sample. As the elastic sheet was not resistant to oil contamination, we replaced the sheet a minimum of every 10 experiments to reduce the extent of swelling.

The initial sample volume, $h_0 L_0 w_0$, was made using a reference guide, as shown in Figs. 2(b) and 2(c). In all experiments, we fixed the initial length $L_0 = 30$ cm, and width $w_0 = 5$ cm, varying only the initial height h_0. The sheet was then compressed uniaxially, with both edges moving at speed $U/2$, to a new length $L = L_0 - Ut$, see Fig. 2(d). Throughout the experiments, the sample height was recorded along the centerline via images of a laser line, taken at an oblique angle, with a resolution of $\approx$19 pixels per mm. The translucent nature of the petroleum jelly means that the laser line can become diffuse. To determine the center of the laser line at each point along the sample, we fitted a Gaussian profile to the red color channel of the image and recorded the location of the mean of the Gaussian as the height $h(x, t)$.

In the experiments we either fixed the height of the layer $h_0 = 5$ mm, and varied the sample compression speed $U \simeq 0.9$–3.9 mm s^{-1}, or we varied the thickness of the initial layer $h_0 = 3$–10 mm and fixed $U \simeq 2$ mm s^{-1}. The aim of the experiments is to investigate how the wavelength and amplitude of the resulting undulations depend on the parameters in the system.

B. Materials

For the experiments we used the viscoplastic fluid petroleum jelly, motivated by previous studies investigating the removal of viscoplastic soil layers from solid surfaces using impinging jets [19,20].

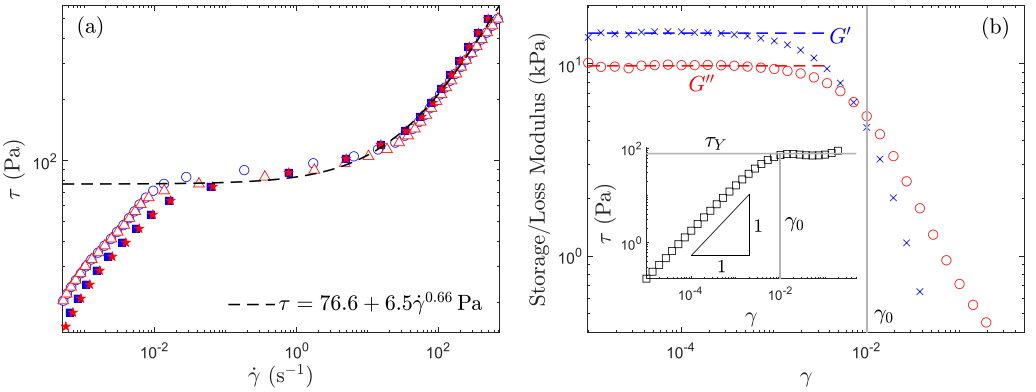


FIG. 3. Petroleum jelly rheometry. In panel (a) the shear stress is plotted against strain rate, from increasing shear stress ramps (30 measurements per decade of shear stress, and a wait of 20 s at each measurement to reach steady state). The black dashed line shows the Herschel-Bulkley best fit [Eq. (1)]. Four separate datasets are given, shown by the different symbols. In panel (b) results of an amplitude sweep are shown, with the storage modulus, G' (blue crosses), and the loss modulus, G'' (red circles), plotted against strain. The blue and red dashed lines indicate average values for small strains ($\gamma < 5 \times 10^{-4}$), with $\bar{G}' = 14.4$ kPa and $\bar{G}'' = 9.7$ kPa, respectively. The gray vertical line shows the critical strain γ_0 when the stress equals the yield stress. The inset shows the shear stress against strain, with gray lines indicating the critical strain and the yield stress. The triangle shows a linear slope, $\tau \propto \gamma$.

Previous studies demonstrating this surface instability used Carbopol, ultrasound gel and hair gel [1–3]. The petroleum jelly is still viscoplastic but allows us to attain higher Bingham numbers, and the translucent nature of the material allows for improved image processing. Rheometer tests were conducted using an Anton Paar Modular Compact Rheometer (MCR) 302. Petroleum jelly has been reported to display thixotropic behavior [21]. We therefore performed creep tests to measure the critical yield stress at which there is an abrupt transition in behavior from elastic creep to viscous flow. We used a parallel plate geometry, attaching 200 grit sandpaper to the plates to limit the effect of slip. We performed shear stress ramps, taking 30 measurements per decade, and waiting 20s at each measurement to attain a steady state. This timescale was chosen as representative of our experiments [22]. Figure 3(a) shows flow curves obtained from four separate measurements of the petroleum jelly. Using a Herschel-Bulkley model fitted after the transition, we find material parameters

$$\tau_y = 76.6 \pm 3.2\,\text{Pa}, \quad K = 6.5 \pm 1.0\,\text{Pa s}^n \quad \text{and} \quad n = 0.66 \pm 0.04, \tag{1}$$

where τ_y is the yield stress, K is the consistency, and n is the power law index.

We also performed an amplitude sweep to measure the storage modulus, G', and loss modulus, G'', as a function of strain; see Fig. 3(b). At low strains, the storage and loss modulus are approximately constant suggesting the material behaves as a linear viscoelastic solid (the inset shows the linear relationship between shear stress and strain). For larger strains, the storage modulus decreases significantly, eventually dropping below the loss modulus, indicating a transition to a fluid like state. The critical strain, $\gamma_0 = 0.01$, at which the stress equals the yield stress aligns with the transition between the storage and loss modulus, suggesting the material can behave in a brittle manner at or below yield. In the linear viscoelastic regime, the average storage modulus is $\bar{G}' = 14.4$ kPa. These results are consistent with rheometry measurements of petroleum jelly in related scraping experiments [20]. We will discuss the consequences of these measured elastic effects in the discussion in Sec. IV.

C. Base state growth

We observed surface undulations in all our compressional experiments. To understand the base-state growth of the layer and provide a reference surface from which to measure undulations, we define the mean height over the sample length $-L/2 \leqslant x \leqslant L/2$ as

$$\bar{h}(t) = \frac{1}{L}\int_{-L/2}^{L/2} h(x,t)\,\mathrm{d}x. \tag{2}$$

We assume that the timescale of the elastic sheet response is much shorter than the timescale in the experiment, and that the elastic sheet is a perfectly incompressible, isotropic material, with Poisson's ratio $\nu = 1/2$. Providing there is a no-slip condition between the sheet and the sample, deformation of the elastic sheet will induce a substrate velocity boundary condition on the sample with velocity in the x direction $u(x, y, z = 0, t) = -Ux/L = -Ux/(L_0 - Ut)$ and with velocity in the y direction $v(x, y, z = 0, t) = Uy/(2L) = Uy/[2(L_0 - Ut)]$, where the center of the sample is assumed to be stationary. In Appendix A we demonstrate the linear dependence on x when stretching the underlying elastic sheet. Assuming this creates a pure compressional flow, i.e., there is no (y, z) dependency in the horizontal velocity u, the mean height of the sample will depend on the compression ratio L/L_0 through

$$\bar{h} = h_0\left(\frac{L}{L_0}\right)^{-1/2} = h_0\left(1 - \frac{Ut}{L_0}\right)^{-1/2}. \tag{3}$$

Mora *et al.* also used this relationship when comparing to experiments uniaxially compressing a viscoelastic fluid with a prestretched elastic substrate [14]. Hence, if measurements of the mean height [Eq. (2)] agree with Eq. (3), then we will infer that the flow is in pure compression, and that the no-slip boundary condition with the elastic substrate is appropriate.

D. Non-dimensional parameters

From the velocity boundary condition, the compression results in a time-dependent strain rate $|\dot{\gamma}_{xx}| = 2U/L(t)$. Using the initial strain rate, we define a Bingham number associated with compression, the ratio of the yield stress to viscous stresses, as

$$\mathrm{Bi} = \frac{\tau_Y}{K\left(\frac{2U}{L_0}\right)^n}. \tag{4}$$

Throughout the two sets of experiments the compressive strain rate is in the range $|\dot{\gamma}_{xx}| = 0.006$–$0.026\ \mathrm{s}^{-1}$, with Bingham numbers $\mathrm{Bi} \sim 130$–340. Given the strain-rates we believe we are beyond the linear viscoelastic behavior below yield (see Fig. 3). As a result, we expect that predominantly viscoplastic deformation is occurring in the experiments. In Sec. IV, we discuss this further and make comparisons between the undulations observed in these experiments, and those observed when scraping a layer of viscoplastic fluid [1–3].

III. RESULTS

We performed two suites of experiments. In the first we kept the thickness of the initial layer fixed at $h_0 = 5$ mm, but varied the speed of compression, U. In the second suite of experiments we varied the layer thickness h_0, but aimed at fixing the speed of compression. Figure 4 summarizes the experimental parameters and average quantities for each of the 39 experiments carried out. In Fig. 4(a) we plot the length of the sample, L, against time, t. Using a linear fit to the data we are able to determine the compression speed, U. Figure 4(b) plots the compression speed, U, and layer thickness, h_0, for each experiment. The color of each marker denotes the Bingham number (or compression speed), with increasing Bingham number from blue to red, as shown by the color bar on the right. The different marker symbols denote different initial layer thicknesses. Note, these marker colors and shapes are also used in Figs. 5, 6, 7, 8, and 10.

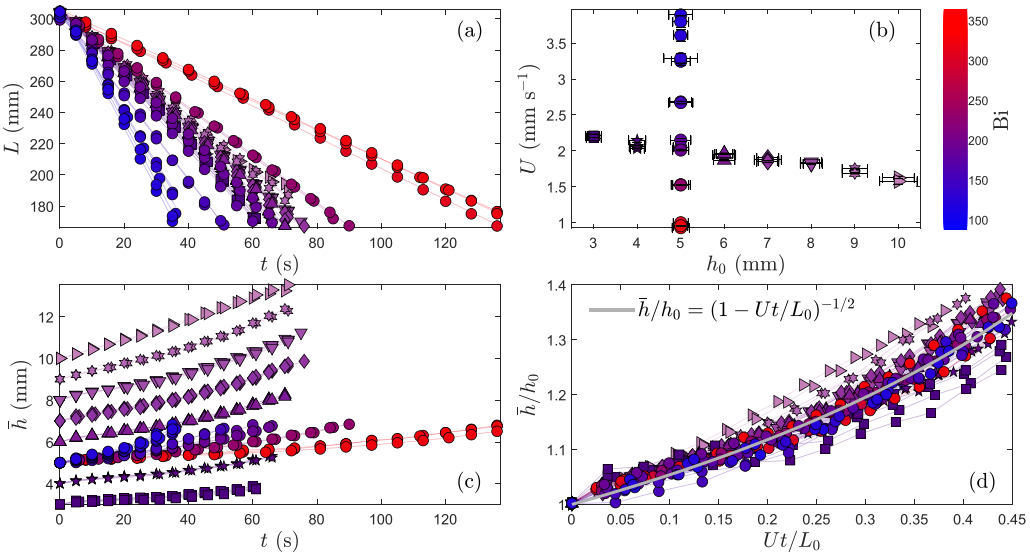


FIG. 4. Experimental parameters for all 39 experiments. (a) Length of the sample, L, against time, t. The solid lines show the linear fits for each experiment. (b) Summary of the experimental parameters. Each data point denotes one experiment, with the prescribed layer thickness h_0, and compression speed U determined from panel (a). The error bars in h_0 are the standard deviation of the initial measured height profile. The error bars in U denote the mean square error of the linear fit, which are smaller than the marker size. Circles indicate a suite of experiments fixing the layer thickness and varying the compression speed, and hence Bingham number, as shown by the color bar on the right-hand side. The remaining purple markers indicate a suite of experiments varying the layer thickness, with opacity increasing with thickness. (c) Mean height, $\bar{h}$, against time, t. (d) Rescaled mean height against dimensionless time. The solid gray line shows Eq. (3). The same marker colors and shapes are also used in Figs. 5, 6, 7, 8, and 10.

By varying the speed at which the clamped edges of the elastic sheet are translated, we are able to compress the sample at different speeds, resulting in different Bingham numbers. For fixed layer thickness, this is a fairly repeatable process as shown by the length of the sample as a function of time in Fig. 4(a), and the corresponding inferred compression speed for repeat experiments, as shown in Fig. 4(b). However, when varying the layer thickness, although we aimed to keep the compression ratio the same by fixing the speed of the clamped edges of the elastic sheet, we observed that the compression speed of the sample decreased. We believe this is evidence of slip at the base of the sample. Assuming a stick-slip behavior, we would expect slip to occur when the wall stress (a material parameter describing the interaction between the fluid and wall) is exceeded [23]. Alternatively, this may be due to presence of bubbles in thicker layers which changes the area of contact with the elastic substrate. For increased layer thicknesses, a domed leading order profile is also observed parallel to the direction of compression, see Fig. 5(f), which suggests that the slip is inhomogeneous throughout the substrate. Despite this, for the layer thicknesses considered, the range of compression speeds measured was narrow, $U = 1.58$–2.21 mm s^{-1}.

Before analyzing the surface undulations in detail, we evaluate the mean height in each experiment. In Figs. 4(c) and 4(d) we plot the mean height, calculated using Eq. (2), against time. To compare with Eq. (3), we then scale the mean height with the initial layer thickness and scale time with the inverse of the initial strain rate, up to a scalar multiple. We see an excellent collapse for most of the experiments suggesting the petroleum jelly is in pure compression. There is, however, a slight trend with layer thickness. We believe this is also evidence of slip at the base in the y direction leading to a larger measured average height for a given compression ratio, $L/L_0 = 1 - Ut/L_0$.

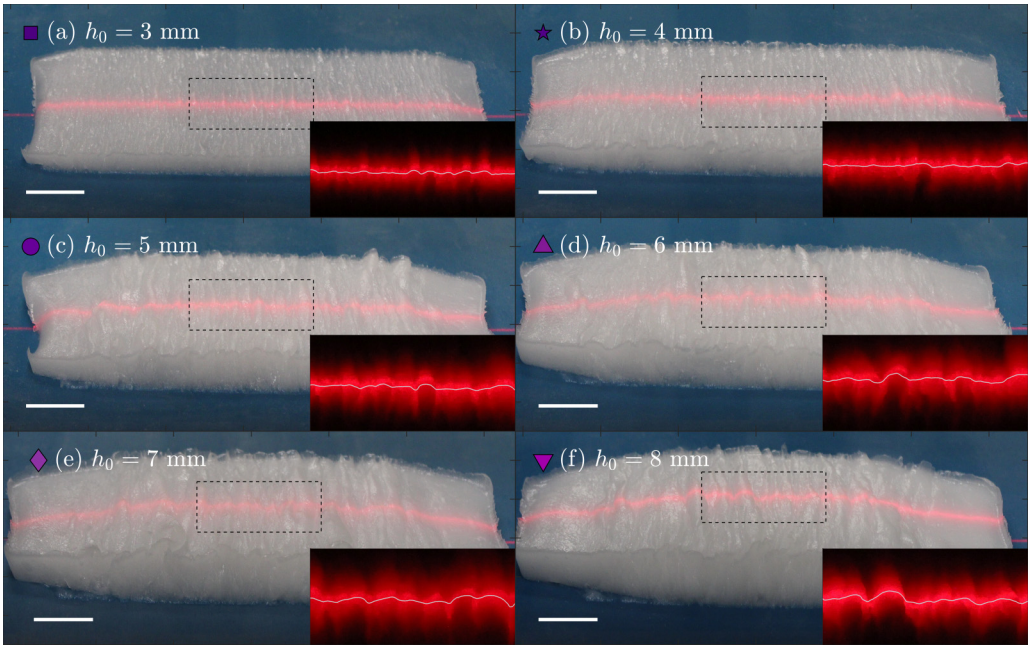


FIG. 5. Experimental photos showing the final snapshot of an experiment for different layer thicknesses (a)–(f) $h_0 = 3$–8 mm, with compression speed $U \sim 2\,\mathrm{mm\ s^{-1}}$. The white horizontal scale bar is 20 mm long. The black dashed boxes show the region replotted in the corresponding insets. The white solid lines show the inferred height profiles.

We first consider the influence of changing the layer thickness. In Fig. 5 we show experimental photos at the end of a set of experiments with different layer thicknesses $h_0 = 3$–8 mm, but with similar compression speeds, $U \sim 2\,\mathrm{mm\ s^{-1}}$ (see Supplemental Material for videos of experiments with layer thicknesses $h_0 = 3$ and 7 mm [24]). From the images we can see there is a clear trend where the scale of features on the surface increases with the initial layer thickness. These images also indicate that the undulations appear to have sharp troughs and smooth crests, characteristics that are somewhat obscured by the diffuse nature of the laser line, but consistent with those observed previously [2], and reminiscent of creases in elastomer films [15,25]. Finally, away from the laser line we can see that the deformation is not purely two-dimensional, with the structure in the y direction increasing with layer thickness.

We next consider the influence of changing the Bingham number. Figure 6 shows the height along the centerline for two different experiments. In Figs. 6(a) and 6(b) experimental photos are shown at the same compression ratio, $L/L_0 \simeq 0.6$, overlain with the inferred height profile; in Figs. 6(c) and 6(d) time series are shown, with time increasing from red to blue. As a first observation, the experiments in Fig. 6 suggest that as we increase the Bingham number, by decreasing the speed of compression, the amplitude of the instability grows, but there is no obvious change in the associated wavelength. In Fig. 6(e) we rescale the time series shown in Fig. 6(c) using the mean height and the length of the sample. The rescaled profiles demonstrate how the undulations are advected inwards by the compressional flow and are formed through amplification of initial irregularities in the surface.

To analyze the height profiles further we pick out two key features: the wavelength of the surface undulations, and the arc length of the profile (total length including undulations). Estimating the wavelength of the instability is challenging because of the inhomogeneous nature of the profile, where, for example, analyzing the Fourier spectrum would bias toward the largest peaks. To overcome this we instead use the findpeaks algorithm in MATLAB, which selects the local maxima [as shown in Figs. 6(c) and 6(d) by the black crosses in the final profile]. To remove any anomalies

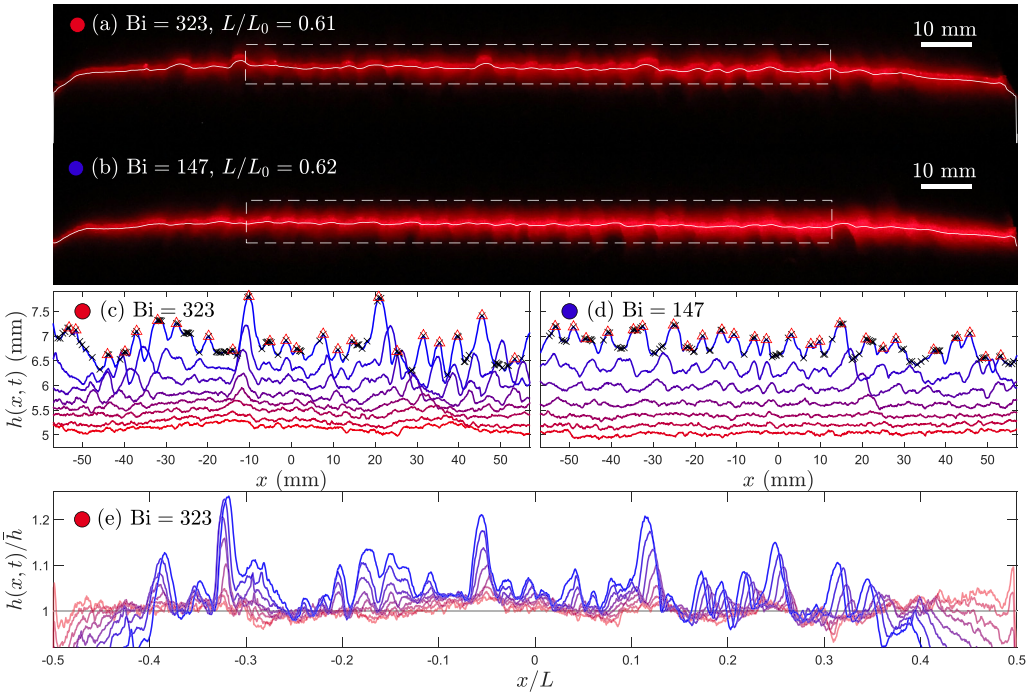


FIG. 6. Varying speed of compression. Height profiles for (a), (c), (e) Bi = 323, $U = 1.0\,\text{mm s}^{-1}$ and (b), (d) Bi = 147, $U = 3.3\,\text{mm s}^{-1}$, with layer thickness $h_0 = 5$ mm. In panels (a), (b) the final image of the experiment is shown overlain by the inferred centerline profile shown as a solid white line. In panels (c), (d) time series of the profiles of the central portion of the profile are shown, given by the white dashed box in panels (a), (b). The corresponding compression ratios are (c) $L/L_0 = [0.98, 0.93, 0.88, 0.83, 0.77, 0.72, 0.66, 0.61]$ and (d) $L/L_0 = [0.96, 0.91, 0.86, 0.80, 0.75, 0.68, 0.62]$ (increasing in time, decreasing in compression ratio, from red to blue). The black crosses on the final blue profiles in panels (c), (d) show the detected local maxima; the red triangles indicate the maxima with a prominence greater than half the mean. In panel (e) the time series in panel (c) is replotted with the horizontal coordinated scaled by the length of the sample, L, and the height scaled by the mean height, $\bar{h}$.

in the selection, we then restrict the peaks to those with a prominence (a measure of how much the peak stands out due to its intrinsic height and its location relative to other peaks) greater than half the mean, which are then indicated by the red triangles in Figs. 6(c) and 6(d).

To find the mean wavelength, we take the distance between the first and last peak, and divide by the total number of peaks. The calculated wavelength, λ, is plotted in Fig. 4(a) against time for all 39 experiments. Initially the wavelength is similar for all experiments with $\lambda \sim 1$ mm. This can be inferred as the residual patterning from setting up the initial condition using the reference guide [see Figs. 2(b) and 2(c)]. The wavelength then increases before plateauing at a range of different values. In Fig. 4(b), we plot the rescaled wavelength, using the initial layer thickness, against dimensionless time. There is now evidence of a collapse, with the data plateauing close to $\lambda/h_0 = 1$ for the largest dimensionless times. To see trends more clearly, we average the wavelength, $\bar{\lambda}$, for dimensionless times $Ut/L_0 \in [0.3, 0.45]$ (chosen as the region where the measure appears to plateau). In Fig. 4(c) we plot the average wavelength against layer thickness, demonstrating a clear linear trend. However, there is a large spread in the data shown by the standard deviation within each experiment, which increases with the initial layer thickness. In Fig. 4(d), we also plot the rescaled average wavelength against Bingham number for experiments with $h_0 = 5$ mm, showing there is no trend with Bingham number for the range of values considered.

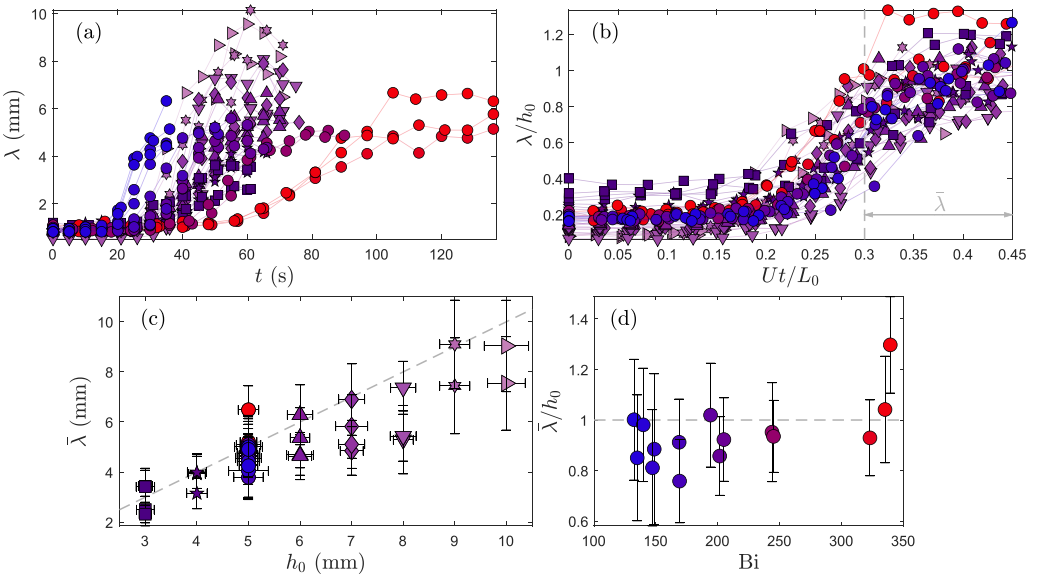


FIG. 7. Wavelength of surface undulations (for details of the marker colors and shapes see Fig. 4). (a) Wavelength λ inferred from the number of peaks plotted against time. (b) Wavelength, scaled by the initial layer thickness, plotted against dimensionless time. The gray arrow indicates the range $Ut/L_0 \in [0.3, 0.45]$ over which the wavelength is averaged. (c) Average wavelength $\bar{\lambda}$ plotted against layer thickness. (d) Average wavelength, scaled with the initial layer thickness, plotted against Bingham number for experiments with $h_0 = 5$ mm. In panels (c), (d) the gray dashed lines plot $\bar{\lambda} = h_0$. We combine the propagating errors to find the standard deviation of the mean wavelength using the standard deviation for λ at each nondimensional time, as seen in the error bars in panels (c), (d).

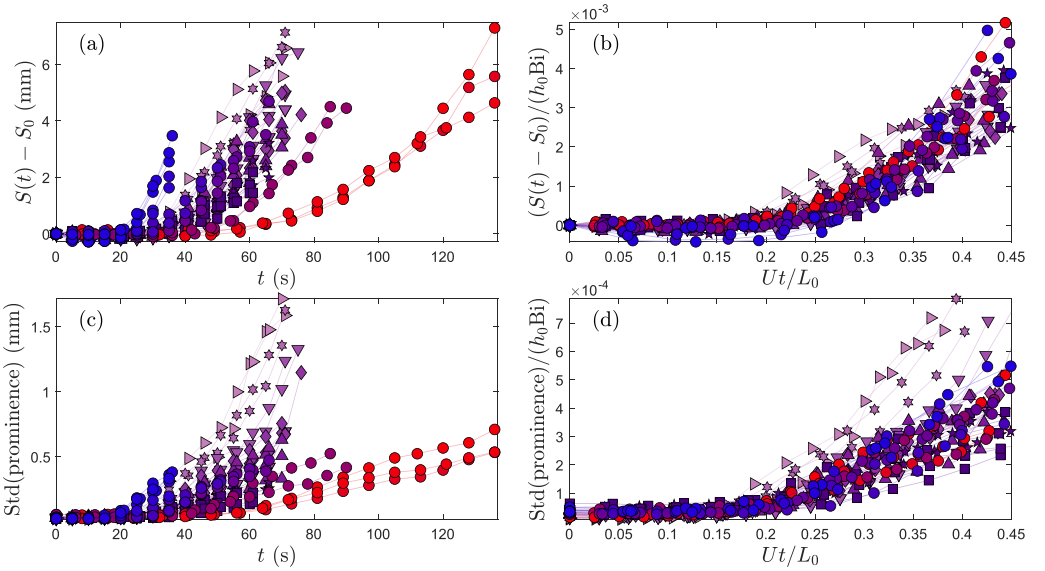


FIG. 8. Arc length of surface undulations (for details of the marker colors and shapes see Fig. 4). (a) The arc length, $S(t)$, relative to the initial arc length, S_0, plotted against time, t. (b) The arc length, scaled by the initial thickness h_0 and the Bingham number Bi, plotted against dimensionless time. (c) Standard deviation of the prominence of peaks plotted against time. (d) Standard deviation of the prominence of peaks, scaled by the initial thickness h_0 and the Bingham number Bi, plotted against dimensionless time.

The arc length, $S(t)$, is calculated over a 11.5-cm-long region in the center of the image, as seen in the profiles in Figs. 6(c) and 6(d). In Fig. 8(a) we plot the increase in the arc length relative to the initial arc length, $S(0) = S_0$, against time. Comparing with the markers in Fig. 4(b), the arc length appears to increase with increasing Bingham number and initial layer thickness. We therefore rescale the arc length with h_0Bi and plot this against dimensionless time, as shown in Fig. 8(b). This rescaling collapses most of the data onto a universal curve. Note that given the variability in the data, we would expect any power law exponent of the Bingham number $\sim$1 would give a similar collapse. Given that the wavelength is independent of changes in the Bingham number, we can view the trend in arc length with Bingham number as a trend in amplitude, with the amplitude increasing as the Bingham number increases. This scaling is consistent with the observation from Fig. 6 that the amplitude of height profiles for Bi = 323 in Figs. 8(a) and 8(c) is larger than for Bi = 147 in Figs. 8(b) and 8(d). A second observation from the height profiles plotted is that the surface undulations become more irregular with increasing Bingham number, with stronger localized peaks appearing. To test this we calculated the standard deviation of the prominence of peaks used to calculate the wavelength; see Figs. 8(c) and 8(d). In both the dimensional and rescaled plots we observe that the standard deviation increases with Bingham number. However, we also observe that the standard deviation strongly increases with initial layer thickness, with the experiments with the largest layer thicknesses, $h_0 = 8,\ 9$, and 10 mm, clear outliers in the rescaled plots.

IV. DISCUSSION

When calculating the wavelength of the surface undulations, the initial wavelength for all experiments is strikingly similar, with a strong cluster around $\lambda \sim 1$ mm; see Fig. 7(a). Although this ensures repeatability across all experiments, its origin remains unclear. The mean peak height of the initial condition is in the range 0.02–0.04 mm, which is at the resolution of the images taken (around 19 pixels per mm). In addition, the clear plateau before the wavelength increases suggests this may be due to resolution. Figure 6(e) demonstrates that subsequent surface undulations are formed through amplifications of the initial irregularities of the surface. To interrogate this further, we performed additional experiments where we patterned the surface with a regular spacing in x and uniform indentation in y, where the depth of the indentation was uncontrolled, see Appendix B. The analyzed wavelengths in Fig. 10(c) show that experiments starting with either the patterned or flat state evolve to the same average wavelength at the end of an experiment (at dimensionless time $Ut/L_0 = 0.45$). Hence, providing the initial patterning wavelength is sufficiently different from the layer thickness, it does not significantly influence the wavelength of the end state. However, the patterning will effect the regularity and arc length, or amplitude, of the final state.

The experiments demonstrate definite trends in the wavelength of the surface undulations with layer thickness. However, there is a spread between repeat experiments and the standard deviation within each experiment, which increases with layer thickness; see Fig. 4(c). We believe this is partly due to the structure observed across the width of the sample, perpendicular to the direction of compression, as seen in Fig. 5 and the videos provided in the Supplemental Material [24]. The structures are not strictly two-dimensional, with the complexity growing with the thickness of the layer. This may be due to the presence of air bubbles in the petroleum jelly, which were challenging to identify for thicker layers; the presence of which is known to initiate the formation of creases in viscoelastic fluids [14].

For all experimental parameters explored, surface undulations were observed, frozen in place by the yield stress of the petroleum jelly. However, we would expect there to be an absence or distinct change in the observations due to the influence of gravitational stresses when the prominence of the peaks is large, and due to an influence of surface tension when the lengthscales are small [14]. Comparing the yield stress to gravitational stresses ($\tau_Y/\rho g\,\Delta h$), taking an approximate density of $\rho = 880\,\mathrm{kg\,m^{-3}}$, we would expect gravitational stresses to play a role when the surface undulations have peaks of height $\Delta h = 9$ mm. From all the experiments, the largest peak height is $\sim$3 mm. Hence, although gravity is not playing a significant role in the current experiments, we would

expect to see an influence at increased Bingham numbers and layer thicknesses. In a similar manner, comparing the yield stress to the Laplace pressure ($\tau_Y \mathcal{L}/\gamma$), taking an approximate value of surface tension of $\gamma = 0.035\,\mathrm{Nm}^{-1}$ [26], we would expect surface tension to play a role on lengthscales of order $\mathcal{L} = 0.5$ mm. As this lengthscale is smaller than the wavelengths observed at late times, we would only expect it to influence the initial surface undulations.

To understand the influence of elasticity, we compare the elastic relaxation time to a typical timescale in the experiments. Consistent with related studies, we define an elastic timescale $t_e = (K/G')^{1/n}$ [3,27,28]. Using the storage modulus measured in either the linear elastic regime or at yielding ($G' = 4.7$ kPa) gives an elastic timescale in the range $8.5 \times 10^{-6}\,\mathrm{s} < t_e < 4.7 \times 10^{-5}\,\mathrm{s}$, which is significantly less than the timescale in our experiments, where the surface undulations evolve on a timescale of 1–10 s. We can compare our experiments with a similar setup uniaxially compressing a layer of a viscoelastic fluid. Mora *et al.* find that the wavelength of surface creases is roughly equal to the initial layer thickness when elasticity is dominant, with deviations at small wavelengths due to surface tension [14]. These findings are consistent with other studies on the growth of a soft layer on a rigid substrate, where confinement in the vertical direction induces a compressive stress under mass addition [29,30]. The wavelength dependence on the layer thickness is consistent with our findings here. However, in the experiments of Mora *et al.*, the undulations evolve on a timescale of 10 ms. In addition, our experiments show rate a dependence where the amplitude depends roughly linearly on the compressive Bingham number, Bi, which is not a function of the elastic properties of the material. These observations and the estimated elastic timescale suggest that elastic effects are largely negligible for the instability described. Finally, from the rheometry data, we see that at the critical strain at which the stress equals the yield stress, there is a transition between the storage modulus and the loss modulus, suggesting the material can behave in a brittle manner below yield. This is consistent with further experiments reversing the motion of the edges putting the sample under tension, where the surface undulations do not disappear but instead open up to form cracks spanning the depth of the material.

Phenomena similar to the surface instability analyzed in these experiments have been observed in experiments scraping viscoplastic layers by Maillard *et al.* [1], Ribinskas *et al.* [2], and Taylor-West and Hogg [3]. In all these experiments, the layer thickness was $O(1)$ cm and the corresponding surface undulations in experimental images were of a similar order of magnitude, although no analysis of the instability observed was performed. However, there are important differences between these experiments and those presented here. In all of the previous experiments, the Bingham number defined using the shear rate (U/h_0) was $O(1)$, significantly smaller than the range considered here. When we replaced the petroleum jelly in our experiments with the viscoplastic fluid used by Taylor-West and Hogg (Enliven Hair Gel Extreme, hold 4), we struggled to image any surface instability due to the small amplitudes. Substituting their material parameters ($\tau_y = 70\,\mathrm{Pa}$, $K = 80\,\mathrm{Pa\,s^n}$ and $n = 0.25$) into the Bingham number, Eq. (4), gives Bingham numbers in the range $\mathrm{Bi} \sim 2.6$–3.7. From the rough scaling predicted in Fig. 8, we would expect the amplitudes to be two orders of magnitude smaller, and hence, below our current resolution. To better understand the dependence on the Bingham number, we would need to change the size by an order of magnitude systematically. One way to change the Bingham number would be to add microcrystalline wax to the petroleum jelly, which allows the yield stress to be tuned, as demonstrated for three-dimensional printing when assembling three-dimensional scaffolds [31].

Another key difference between the scraping experiments [1–3] and those described here is the uniformity of compression. In our experiments, using an elastic substrate to uniaxially compress the sample leads to a uniform compressive stress throughout the domain. In contrast, particle image velocimetry measurements from Ribinskas *et al.* [2] suggested that the undulations formed at the nose of the profile and were then propagated backwards with little deformation. In their thin film model, the gradient and curvature of the free surface control the compressive stress, which at late times is maximized near the nose of the profile.

We can also compare our experiments with the related problem of a slumping, two-dimensional column by Liu *et al.* [4]. Using numerical simulations, they considered a Bingham fluid collapsing

vertically under its own weight. In this case, the velocity of the column is nonuniform (starting and ending at rest), gravitational forcing is parallel to the direction of compression, and a free-slip condition is applied alongside the layer. Nonetheless, comparing their profiles (their Fig. 8) for different Bingham numbers at the same degree of compression, the amplitude increases with increasing Bingham number. In addition, their computations show that the wavelength of surface undulations scales roughly with the width of the column and that changing the Bingham number does not influence the wavelength. Liu *et al.* rationalize their numerical results at initiation by comparing with plasticity results given by slipline theory, which predicts that the initial deformation should have a lengthscale that is twice the thickness of the layer. This corroborates the linear dependence on the layer thickness but is twice the wavelength observed in these experiments. We believe the main reason for this is the differing boundary condition alongside, or in our setup, underneath the compressed layer that controls geometry of the slipline field. But investigating the uniaxial compression of a perfectly plastic material numerically is required to understand this difference.

V. CONCLUSION

In this paper we have characterized for the first time a surface instability that occurs when a yield stress fluid is subject to uniaxial compression. Our experiments using petroleum jelly have shown that the amplitude of surface undulations depends linearly on the Bingham number, whereas the wavelength is approximately equal to the initial thickness of the compressed layer.

In future, we would like to develop the experimental setup to remove the large variability between experiments, which may come from the additional structure observed across the width of the sample. This would allow us to investigate more subtle aspects of the instability, such as the transient evolution of the surface undulations before the wavelength plateaus. In addition, all the experiments carried out were at large Bingham numbers, without the influence of surface tension and gravitational stresses. It would be interesting to move to lower Bingham numbers to test the proposed scaling laws and see the influence of surface tension. To compare with the experiments, numerical simulations should also be carried out for both this setup of uniaxial compression of a viscoplastic layer, and for the setup of scraping a thin film of viscoplastic fluid, which Ribinskas *et al.* [2] and others previously considered.

Finally, motivation for these experiments stems from the geophysical application of understanding short-wavelength faulting features in accretionary wedges. Building on this study there are two key areas we would like to explore: the effect of nonuniform initial layer thickness and the effect of the boundary condition between the layer and the rigid substrate. Initial accretionary wedge geometry is known to be better represented by a tapered sediment thickness rather than a uniform layer thickness [12]. Our observations suggest that the surface undulations would therefore vary in wavelength along the taper. In addition, from comparing the experiments scraping a layer of viscoplastic fluid [1–3], the numerical results of a slumping viscoplastic column [4], and our experiments presented here, it is clear that the bottom boundary condition parallel to the direction of compression has a significant effect on the surface undulations. This has strong analogies to the inferred basal friction in accretionary wedges, where numerical models have suggested that fault spacing decreases with increasing basal friction [32]. Both of these areas require future exploration with experimental and numerical techniques to fully understand their influence on the surface instability observed.

ACKNOWLEDGMENTS

T.V.B. acknowledges the support of P. Thomas and the Fluid Dynamics Research Centre at the University of Warwick. T.V.B. also thanks A. Hutchinson, J. Neufeld, C. Penney, and E. Ribinskas for helpful discussions and reading through the manuscript. During the project, T.V.B. was supported by the Leverhulme Trust Early Career Fellowship (Grant No. ECF-2022-584).

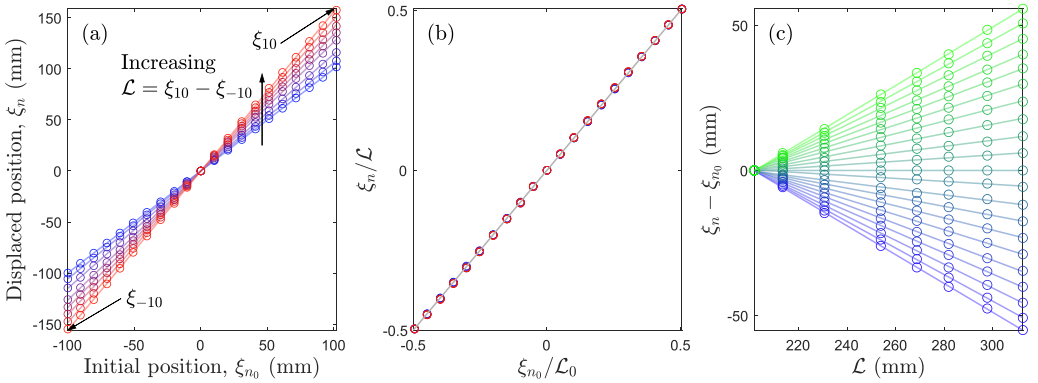


FIG. 9. Uniform tension of underlying elastic sheet. (a) Displaced position of markers, ξ_n, against initial position, ξ_{n_0}, for increasing total length between the first and last marker, $\mathcal{L} = \xi_{10}$–ξ_{-10}, from blue to red. Solid lines are the linear best fits for each $\mathcal{L}$. (b) Displaced position, scaled with $\mathcal{L}$, against initial position, scaled with $\mathcal{L}_0 = \xi_{10_0}$–$\xi_{-10_0}$. Solid gray line plots $\xi_n/\mathcal{L} = \xi_{n_0}/\mathcal{L}_0$. (c) Displacement of markers, ξ_n–ξ_{n_0}, against total length (increasing n from blue to green). Solid lines are linear best fits for the nth marker.

DATA AVAILABILITY

The data that support the findings of this article are publicly available [33].

APPENDIX A: UNIFORM TENSION OF UNDERLYING ELASTIC SHEET

In Sec. II C we assume that the underlying elastic sheet is uniform with a horizontal velocity, u, that is linear in x. To demonstrate this, we carried out an additional experiment tracking markers on the surface as the sheet is stretched. When the sheet is undeformed, we placed linearly spaced markers at $\xi_{n_0} = 10n$ (mm), for $n \in [-10, 10]$, along the centerline of the sheet. We then stretched the sheet by an increasing amount of strain and tracked the displaced position of the markers, ξ_n. In Fig. 9, we plot the displaced position of each marker against the initial position and the total length of the markers, $\mathcal{L} = \xi_{10} - \xi_{-10}$. Figures 9(a) and 9(b) show that the initially linear distribution of markers remains linear as the elastic sheet is stretched. Figure 9(c) shows that the displacement of each marker is linear with the total length of the markers $\mathcal{L}$.

APPENDIX B: PATTERNED INITIAL CONDITIONS

To test the influence of the initial condition, we carried out an additional experiment where we patterned the surface with an indentation at regular intervals in x, uniform in y; see Fig. 10. The comb used had a uniform spacing of ∼5.8 mm, however the depth of the indentation was not controlled. We carried out two experiments, one where we patterned the entire sample, for all x, and one where we patterned half of the sample, for $x < 0$, and used the normal procedure to scrape the remaining half flat.

Figures 10(a) and 10(b) show time series of the height profiles. Selecting the peaks, as described previously, we infer a wavelength at each time. For the case where we pattern half the surface, we split the domain in half and calculate two wavelengths. In panel (c) the inferred wavelength, scaled relative to the initial layer thickness, is plotted against dimensionless time. We also plot repeats of experiments where the surface is scraped flat for all x, replotted from Figs. 4–8. Initially it is clear that the wavelength from the patterned surface is much larger than those with a flat initial condition. However, at later times the wavelengths both converge to close to $\lambda/h_0 = 1$. These experiments demonstrate that provided the wavelength of the initial patterning is sufficiently different from the layer thickness, it does not significantly influence the wavelength of the end state. However,

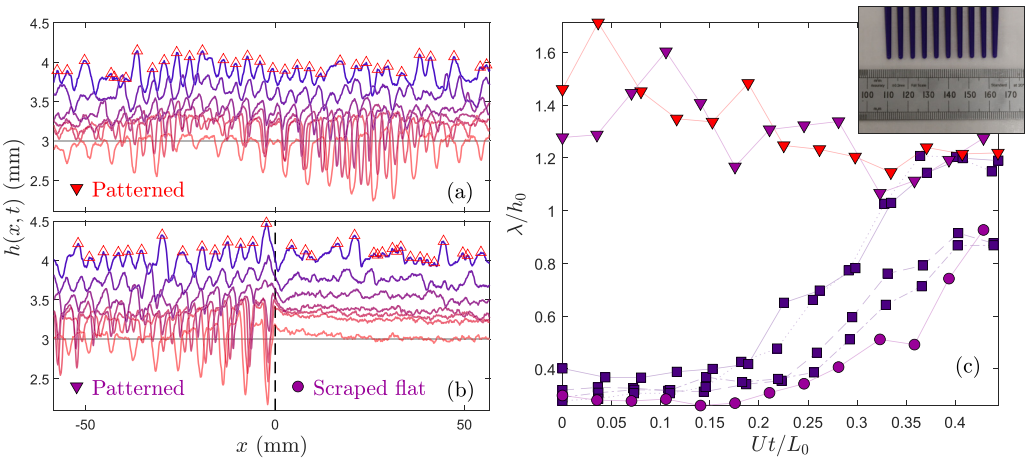


FIG. 10. Patterned surfaces. Height profiles for (a) an initial condition which is patterned for all x, and (b) an initial condition which is patterned for $x < 0$, with Bi $= 193$, $U = 2.2\,\text{mm s}^{-1}$, $h_0 = 3$ mm. The red triangles indicate the maxima with a prominence greater than half the mean. The black dashed line in panel (b) shows the transition between the patterned and scraped-flat initial condition. (c) Inferred wavelength, scaled relative to the initial layer thickness, plotted against dimensionless time. The triangles and circles are inferred wavelengths from panels (a), (b). The blue squares refer to repeat experiments shown in Figs. 4–8. Inset shows an image of the comb used to generate the patterned surface, with ruler for scale.

the patterning does influence the arc length and regularity of the pattern; see, for example, the comparison between the patterned and scraped flat regions in Fig. 10(b).

[1] M. Maillard, C. Mézière, P. Moucheront, C. Courrier, and P. Coussot, Blade-coating of yield stress fluids, J. Non-Newtonian Fluid Mech. **237**, 16 (2016).
[2] E. Ribinskas, T. V. Ball, C. E. Penney, and J. A. Neufeld, Scraping of a viscoplastic fluid to model mountain building, J. Fluid Mech. **998**, A58 (2024).
[3] J. J. Taylor-West and A. J. Hogg, Scraping of a thin layer of viscoplastic fluid, Phys. Rev. Fluids **9**, 053301 (2024).
[4] Y. Liu, N. J. Balmforth, S. Hormozi, and D. R. Hewitt, Two-dimensional viscoplastic dambreaks, J. Non-Newtonian Fluid Mech. **238**, 65 (2016).
[5] T. V. Ball, C. E. Penney, J. A. Neufeld, and A. C. Copley, Controls on the geometry and evolution of thin-skinned fold-thrust belts, and applications to the Makran accretionary prism and Indo-Burman ranges, Geophys. J. Int. **218**, 247 (2019).
[6] G. Grando and K. McClay, Morphotectonics domains and structural styles in the Makran accretionary prism, offshore Iran, Sediment. Geol. **196**, 157 (2007).
[7] P. Maneerat and R. Bürgmann, Geomorphic expressions of active tectonics across the Indo-Burma range, J. Asian Earth Sci. **223**, 105008 (2022).
[8] S. H. Emerman and D. L. Turcotte, A fluid model for the shape of accretionary wedges, Earth Planet. Sci. Lett. **63**, 379 (1983).
[9] J. Gratton and C. Alberto Perazzo, Self-similar asymptotics in convergent viscous gravity currents of non-Newtonian liquids J. Phys.: Conf. Ser. **166**, 012011 (2009).
[10] E. B. Burov, Rheology and strength of the lithosphere, Mar. Pet. Geol. **28**, 1402 (2011).
[11] J. Panian and D. Wiltschko, Ramp initiation in a thrust wedge, Nature (London) **427**, 624 (2004).

[12] J. Panian and D. Wiltschko, Ramp initiation and spacing in a homogeneous thrust wedge, J. Geophys. Res.: Solid Earth **112**, 2004JB003596 (2007).
[13] X. Guan, L. Reddipalli, D. T. Butler, Q. Liu, and S. S. Velankar, Rate-dependent creasing of a viscoelastic liquid, Extreme Mech. Lett. **55**, 101784 (2022).
[14] S. Mora, M. Abkarian, H. Tabuteau, and Y. Pomeau, Surface instability of soft solids under strain, Soft Matter **7**, 10612 (2011).
[15] S. Cai, D. Chen, Z. Suo, and R. C. Hayward, Creasing instability of elastomer films, Soft Matter **8**, 1301 (2012).
[16] D. Chen, S. Cai, Z. Suo, and R. C. Hayward, Surface energy as a barrier to creasing of elastomer films: An elastic analogy to classical nucleation, Phys. Rev. Lett. **109**, 038001 (2012).
[17] S. Chatterjee, C. McDonald, J. Niu, S. S Velankar, P. Wang, and R. Huang, Wrinkling and folding of thin films by viscous stress, Soft Matter **11**, 1814 (2015).
[18] X. Guan, A. P. Sarma, E. Kakarla Hamesh, J. Yang, N. Nguyen, E. Cerda, L. Pocivavsek, and S. S. Velankar, Compression-induced buckling of thin films bonded to viscous substrates: Uniform wrinkles vs localized ridges, Int. J. Solids Struct. **254–255**, 111843 (2022).
[19] R. R. Fernandes, D. Oevermann, and D. I. Wilson, Cleaning insoluble viscoplastic soil layers using static and moving coherent impinging water jets, Chem. Eng. Sci. **207**, 752 (2019).
[20] J.-H. Tsai, R. R. Fernandes, and D. I. Wilson, Measurements and modelling of the 'millimanipulation' device to study the removal of soft solid layers from solid substrates, J. Food Eng. **285**, 110086 (2020).
[21] P. Coussot, Q. D. Nguyen, H. T. Huynh, and D. Bonn, Viscosity bifurcation in thixotropic, yielding fluids, J. Rheol. **46**, 573 (2002).
[22] D. Bonn, M. M. Denn, L. Berthier, T. Divoux, and S. Manneville, Yield stress materials in soft condensed matter, Rev. Mod. Phys. **89**, 035005 (2017).
[23] M. Daneshi, A. Pourzahedi, D. M. Martinez, and D. Grecov, Characterising wall-slip behaviour of Carbopol gels in a fully-developed Poiseuille flow, J. Non-Newtonian Fluid Mech. **269**, 65 (2019).
[24] See Supplemental Material at http://link.aps.org/supplemental/10.1103/x9t6-4324 for videos of experiments with initial layer thicknesses $h_0 = 3$ and 7 mm, and compression speeds $U \sim 2.2$ and 1.9 mm s^{-1}, respectively.
[25] W. Hong, X. Zhao, and Z. Suo, Formation of creases on the surfaces of elastomers and gels, Appl. Phys. Lett. **95**, 111901 09 (2009).
[26] L. J Forney and L. A Spielman, Aerosol rebound from viscous coatings in turbulent flow, J. Colloid Interface Sci. **52**, 468 (1975).
[27] L.-H. Luu and Y. Forterre, Drop impact of yield-stress fluids, J. Fluid Mech. **632**, 301 (2009).
[28] J. van der Kolk, D. Tieman, and M. Jalaal, Viscoplastic lines: Printing a single filament of yield stress material on a surface, J. Fluid Mech. **958**, A34 (2023).
[29] M. Ben Amar and P. Ciarletta, Swelling instability of surface-attached gels as a model of soft tissue growth under geometric constraints, J. Mech. Phys. Solids **58**, 935 (2010).
[30] B. Li, Y.-P. Cao, X.-Q. Feng, and H. Gao, Mechanics of morphological instabilities and surface wrinkling in soft materials: A review, Soft Matter **8**, 5728 (2012).
[31] D. Therriault, R. F. Shepherd, S. R. White, and J. A. Lewis, Fugitive inks for direct-write assembly of three-dimensional microvascular networks, Adv. Mater. **17**, 395 (2005).
[32] G. Ito and G. F. Moore, Widths of imbricate thrust blocks and the strength of the front of accretionary wedges and fold-and-thrust belts, Tectonophysics **799**, 228704 (2021).
[33] T. Ball, Data for Uniaxial compression of a yield stress fluid. University of Warwick, Dataset, 2026, https://doi.org/10.82444/warw.34021944.v1.